Texture and microstructure evolution during non-crystallographic shear banding in a plane strain compressed Cu–Ag metal matrix composite

N. Jia [a,*], D. Raabe [b,*], X. Zhao [a]

[a] *Key Laboratory for Anisotropy and Texture of Materials (MOE), Northeastern University, Shenyang 110819, People's Republic of China*
[b] *Max-Planck-Institut für Eisenforschung, D-40237 Düsseldorf, Germany*

Abstract

We studied the texture and microstructure evolution in a plane strain compressed Cu–Ag metal matrix composite (MMC) with a heterophase microstructure using crystal plasticity finite element simulations. Lattice reorientations induced by both crystallographic (dislocation slip and twinning) and non-crystallographic (shear banding) mechanisms are addressed. First, simulations on a polycrystalline composite are made. Quite similar texture trends are observed for the composites and for the individual single-phase materials, namely, copper-type texture components in the Cu phase and brass-type texture components in the Ag phase. This result differs from experimental data that show less copper-type and more brass-type textures in both phases for the composite materials. To explore co-deformation mechanisms that lead to the specific crystallographic textures in the MMC, bicrystal simulations for the composite with specific initial orientation combinations are performed. The bicrystal simulations reproduce the experimentally observed trends of texture evolution in the respective phases of the composite, indicating that the localized stress and strain fields as well as the co-deformation mechanisms within the actual heterophase microstructure are well captured. The modeling shows that to accommodate plastic deformation between adjacent phases in the bicrystals, pronounced shear bands are triggered by stress concentration at the hetero-interfaces. With further deformation the bands penetrate through the phase boundaries and lead to larger lattice rotations. The simulations confirm that the shear banding behavior in heterophase composites is different from that in single-phase metals and the texture evolution in composite materials is strongly influenced by the starting texture, the local constraints exerted from the phase boundaries and the constitutive properties of the abutting phases.

1. Introduction

Shear banding in plastically strained metallic materials is an important topic owing to the complex interaction of crystallographic and non-crystallographic deformation mechanisms. It is the most frequently observed yet least understood mesoscopic deformation phenomenon in high-performance materials [1–18]. Shear bands, in the form of non-crystallographic band-like regions of concentrated plastic flow, set in when homogeneous dislocation slip or twinning is inhibited [7–9,14,18]. The bands start in individual crystallites but proceed across multiple interfaces and finally cover a large volume fraction of the entire microstructure [1,8,9]. Owing to the non-crystallographic alignment of the bands, they add additional degrees of freedom to the total deformation field. On the other hand, shear bands represent a type of deformation mechanism that involves very high dislocation (or twin) densities

* Corresponding authors.
  E-mail addresses: jian@atm.neu.edu.cn (N. Jia), d.raabe@mpie.de (D. Raabe).

locally inside them and at their rims. The regions surrounding them are much less strained, typically by one to three orders of magnitude [10,12]. Substructure evolution and development of shear bands are strongly influenced by the stacking fault energy (SFE), as confirmed by a number of experiments [1,7–9,14,18]. According to the terminology of Wagner et al. [5], low-SFE materials with a pre-existing microstructure consisting of twin-matrix lamellae produce brass-type shear bands, and high-SFE metals with a microstructure consisting of elongated dislocation walls and cell blocks produce copper-type shear bands. Therefore, shear banding is preceded by the formation of planar obstacles that are determined by the SFE and by the crystallography of homogeneous dislocation slip.

Shear banding, although appearing as a non-crystallographic deformation mechanism, is also associated with large local crystallographic reorientations, i.e. texture changes. Such local crystallographic orientations of deformed face-centered cubic (fcc) and body-centered cubic (bcc) metals have been characterized using transmission electron microscopy (TEM) [3,13,15,19]. It was found that in both types of materials the shear banding induced texture evolution is profoundly different from crystal rotation that originates from homogeneous dislocation and twinning shear alone. For fcc metals, activation of shear banding produces the weaker copper ($\{112\}\langle111\rangle$) and S ($\{123\}\langle634\rangle$) texture components (copper-type textures) as well as the stronger Goss ($\{011\}\langle100\rangle$) and brass ($\{011\}\langle211\rangle$) texture components (brass-type textures) compared to regions outside the shear bands. For bcc metals, the strain concentration in shear bands causes a rotation of the in-band crystal volume around the $\langle110\rangle$ crystal axis which is parallel to the transverse direction of the cold rolled sample. Although the shear banding induced textures in single-phase metals have been studied in great detail, corresponding studies on multi-phase metal matrix composites (MMCs) with a microstructure constituting heterophase interfaces are rarely conducted. Actually, most of the deformation texture studies on multiphase metallic materials so far were conducted by experiments and a number of interesting results have been obtained [20–28]. In a two-phase TiAl alloy consisting mainly of lamellar γ and α_2 grains [22], the brass-type rolling texture was observed in the γ-matrix when the alloy was subjected to two different deformation modes, i.e. compression at room temperature and hot extrusion. The result was unexpected and it was explained in terms of the fact that in both types of processing a strong tendency prevailed to deform via plane strain condition, due to the influence of the α_2 lamellae on the slip and twinning geometry in the matrix. Studies on Cu–Nb multilayer composites with different layer thicknesses (ranging from submicron to nanometer in scale) during accumulative roll bonding [24,27,28] revealed that the textures developed in Cu and Nb layers were distinctly different from classical rolling textures frequently observed in their single-phase counterparts, both by experiment [1–9] and by simulation [29–38]. It was suggested that the Cu/Nb interfaces influenced the slip activity

in both phases by constraining grain deformation or through the kinetics of dislocation–interface interactions. Although all these studies have clearly shown that in composite materials heterophase interfaces play a major role in the texture development of the constituent phases, an understanding of how through-interface shear banding accommodates the imposed deformation and the effect of shear banding on texture evolution is still lacking.

Hence, our aim here is the numerical simulation of texture evolution in a composite consisting of two immiscible metals, Ag as matrix and Cu as second phase, under plastic deformation. The Cu–Ag sheet after cold rolling to large strains can be used as a high-strength conductive material, as refinement of the microstructure leads to a high strength [11,39–41]. As mentioned above, in the mechanically processed composites, textures can be sensitively influenced by the presence of a massive volume fraction of a second phase [20,24,26–28]. However, less effort has so far been made towards modeling the phase-to-phase interactions for predicting the evolution of preferred grain orientation distributions and strain accommodation of shear banded regions [42,43]. Therefore, in this work plane strain compression of polycrystal and bicrystal Cu–Ag composite is simulated using a crystal plasticity finite element (CPFE) framework that incorporates the non-crystallographic shear banding mechanism in addition to dislocation slip and mechanical twinning [16]. Both types of deformation micromechanisms (crystallographic and non-crystallographic) and the associated lattice reorientations in the heterophase composite microstructure are addressed. The layout of the paper is as follows: First, the crystallographic textures obtained from polycrystal simulations for the Cu–Ag composite are presented. Discrepancies between predictions and experimental data from the literature are found. To explore co-deformation mechanisms that lead to specific crystallographic textures in the MMC, bicrystal simulations for the composite with specific and ideal initial orientation combinations are performed. Next we analyze the inhomogeneity of the resulting microstructures and plastic flow in the bicyrstals. Specifically, we address the observation that compared to single-phase materials the composites are more prone to undergoing shear banding. This phenomenon is discussed in terms of the existence of heterophases. Finally, polycrystal simulations incorporating more non-crystallographic shear in one of the individual phases of the composite are presented. This latter test is conducted to demonstrate that for modeling deformation textures in a heterophase microstructure, stress and strain localization effects exhibit a strong influence on the shear banding behavior.

2. Simulation procedures

2.1. Constitutive formulations

A CPFE model is used to simulate the texture evolution in Cu–Ag heterophase composites during plane strain

compression. The model is based on a constitutive model that incorporates shear banding as a separate non-crystallographic deformation mechanism in conjunction with and competing to dislocation slip and mechanical twinning [44]. The implementation of the different deformation mechanisms follows the recent work of Jia et al. [16]. For shear banding as a collective, third type of deformation mechanism, we use and refer to the model developed by Anand and Su [45] for amorphous metallic materials.

2.2. Constitutive material parameters

The constitutive parameters for the individual Cu and Ag phases are determined by fitting the macroscopic stress–strain curves obtained from uniaxial tensile tests conducted on each pure metal [46,47]. The experimentally available data on the pure metals from literature show very ductile behavior in the annealed and coarse-grained form. The material parameters used in this study thus represent values of the individual phases with micrometer-sized grains in the two-phase composite. The use of such fitted data for the respective pure phases is justified since at the modest deformations simulated here mutual chemical mixing can be neglected. The fitted parameters are listed in Table 1. For the two fcc phases, 12 $\{111\}\langle110\rangle$ dislocation slip systems and 12 $\{111\}\langle112\rangle$ twinning systems are considered.

2.3. FEM implementation

Based on the constitutive laws outlined above, CPFE simulations are carried out using the finite element solver MSC.Marc2010 together with a user defined material subroutine [16,44]. This paper firstly focuses on the texture simulation of fcc–fcc (Cu–Ag) heterophase composite under plane strain compression by using a polycrystal model. For further studying shear banding in such materials with heterophase interfaces in more micromechanical detail as a function of crystal orientation, the deformation of fcc Cu plus fcc Ag bicrystals with varying initial orientations is simulated. For the bicrystal modeling, detailed

results on local orientation distributions, shear band topology and the governing micromechanisms are presented.

3. Polycrystal simulations of texture evolution

3.1. Polycrystal model

For simulating texture evolution of the polycrystalline Cu–Ag composite, a finite element mesh including 2000 eight-noded, isoparametric, three-dimensional brick elements is used for the composite. Different material properties representing different single-phase metals are given to the respective elements so that the overall composition of the fcc–fcc composite is Cu–68.3 vol.% Ag or Cu–60.1 at.% Ag [48]. The elements of the different phases are clustered in random order in the composite. By assigning one orientation to each of the eight integration points in an element before deformation, the numbers of initial orientations representing random textures of the constituent phases in the as-received material are 5120 (640×8) for Cu and 10,880 (1360×8) for Ag. As loading state, plane strain compression at a strain rate of 10^{-3} s^{-1} in conjunction with periodic boundary conditions is simulated to approximate the deformation state in the inner (mid-thickness) layers of a cold rolled specimen [20,49].

3.2. Texture evolution predicted by polycrystal modeling

As orientations that occur during plane strain compression of materials with cubic symmetry are concentrated along certain directions in Euler space, specific fibers in Euler space for each constituent phase in the Cu–Ag composite are used to characterize the texture evolution in the respective phases with increasing thickness reduction [2,4,50].

For the fcc phases in the composite, the simulated orientation densities along the α and β fibers are presented in Fig. 1 [2,4,5,51]. The texture simulations for single-phase Cu and Ag with random initial textures are also presented for comparison. To simplify the presentation, Miller indices and Euler angles of some ideal rolling texture compo-

Table 1

Material parameters of the Cu and Ag phases used in the crystal plasticity simulations. C_{11}, C_{12} and C_{44} are the single crystal elastic constants. D_0 and Q_{SD} denote the bulk diffusion coefficient and the activation energy for dislocation climb, respectively. The following parameters are used for all phases: initial dislocation density $\rho_{sgl,0} = 1.0 \times 10^{12}$ m^{-2}, dipole density $\rho_{dip,0} = 1.0$ m^{-2}, initial glide velocity $v_0 = 1.0 \times 10^{-4}$ m s^{-1}, and reference shear rate of the shear band systems $\dot{\gamma}_0^\chi = 1.0 \times 10^{-4}$ m s^{-1}. The asterisk (*) indicates fitting parameters.

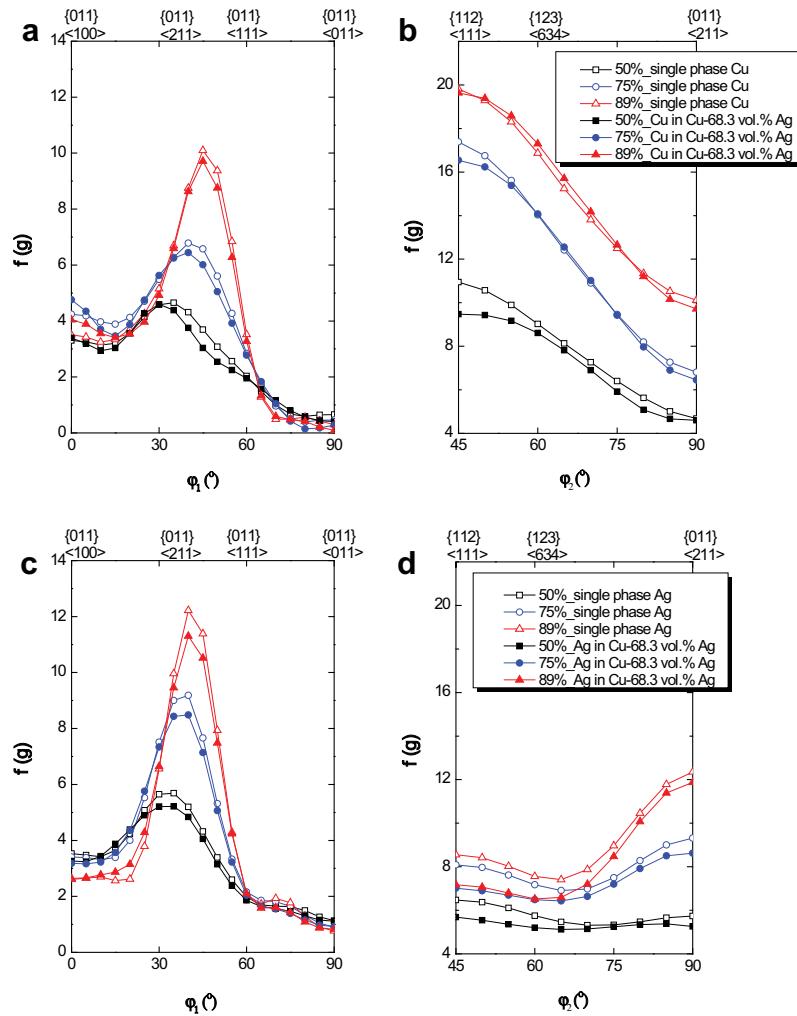| Phase	C_{11} (GPa)	C_{12} (GPa)	C_{44} (GPa)	d_{grain} (μm)	b (m)	D_0 (m^2 s^{-1})
Cu	168.4	121.4	75.4	30	2.55×10^{-10}	2.0×10^{-5}
Ag	124.0	93.1	46.1	30	2.88×10^{-10}	4.0×10^{-5}
	τ_{solute} (GPa)*	Q_{SD} (J)*	Q_0 (J)*	p^*	q^*	s (μm)
Cu	0.0142	2.7×10^{-19}	4.0×10^{-19}	1.03	1.0	0.15
Ag	0.0048	3.4×10^{-19}	3.58×10^{-19}	1.15	1.0	0.15
	b_{twin} (m)	L_0^*	$\dot{N}_0$ (s^{-1})*	r^*	γ_{sf} (J m^{-2})	$\hat{\tau}_{sb}$ (GPa)*
Cu	1.47×10^{-10}	$520 \times b$	1.0×10^{14}	2.0	0.042	0.184
Ag	1.66×10^{-10}	$520 \times b$	2.0×10^{15}	2.0	0.016	0.112

Fig. 1. Predicted texture evolution of cold rolled pure metals and Cu–68.3 vol.% Ag composite at different thickness reductions in fiber representation: (a) α and (b) β fiber for single-phase Cu and Cu phase in the composite, (c) α and (d) β fiber for single-phase Ag and Ag phase in the composite. The α fiber is placed at the Euler space section with constant angles $\Phi = 45°$ and $\varphi_2 = 0°$; the β fiber is a skeleton fiber, i.e. it follows the local maximum texture intensity $f(g)$ in each Euler space section along the φ_2 angle.

Table 2
Miller indices and Euler angles of the ideal texture orientations in fcc metals.

Component	Indices $\{hkl\}\langle uvw \rangle$	Bunge (φ_1, Φ and φ_2)
Copper	$\{112\}\langle111\rangle$	90°, 35°, 45°
Goss	$\{011\}\langle100\rangle$	0°, 45°, 0°
Brass	$\{011\}\langle211\rangle$	35°, 45°, 0°
S	$\{123\}\langle634\rangle$	59°, 37°, 63°

nents are listed in Table 2 [1–5,52]. At 50% thickness reduction, the Goss, brass and copper texture components are predicted in both phases of the composite. This agrees with experimental observations for pure Cu and Ag polycrystals [1,4,53,54]. However, after 50% deformation, differences between the two phases start to appear. This can be seen on the α fiber in terms of the brass component and on the β fiber in terms of the copper component: after 75% thickness reduction a more significant increase of the brass and Goss components and a less pronounced increase of

the copper and S components are predicted in the Ag phase compared to the Cu phase. When the thickness reduction reaches 89%, in the Cu phase the copper component further develops and very sharp copper-type texture appears. In the Ag phase, the brass component is more significantly strengthened compared to the copper component as a function of deformation, which contributes to a dominant brass-type texture. The predicted texture evolution in the two phases of the composite shows quite similar trends as that of their respective single-phase counterparts. Nevertheless, while the simulation of the Ag phase agrees well with bulk X-ray diffraction texture measurement, the predicted result for the Cu phase deviates from the measurements of the same composite which exhibit a stronger brass component compared to the copper component in Cu at 75% and higher rolling reductions [26]. More specifically, the measured texture development in the Cu phase of the composite is very different from the copper-type textures expected for rolled pure metals with medium or high SFEs [1–5]. Thus, it is obvious that the existence of the Ag

phase or Cu–Ag heterophase interfaces plays a role for the texture evolution of the Cu phase when embedded into the composite. However, this feature is not captured by the current modeling approach, and will be analyzed in more detail below.

4. Bicrystal heterophase simulations of orientation distribution

4.1. Bicrystal models

For bicrystal simulations, the modeled region is a portion of a bulk material with thickness H_0 and length L_0 in the undeformed state, as shown in Fig. 2. The fcc-plus-fcc heterophase bicrystal model comprises the mutually stacked Cu and Ag crystals. To mimic an initial eutectic composition of Cu–68.3 vol.% Ag [48], the thickness ratio between Cu and Ag crystals is 3:6.5. For the whole model, the thickness-to-length ratio, i.e. H_0:L_0, is 2.0. Plane strain compression is used as an approximation of the deformation in the mid-thickness layers of an actual rolling process. The elongation direction (ED), normal direction (ND) and transverse direction (TD) are set to coincide with a Cartesian coordinate system, X, Y and Z, respectively. A prescribed displacement corresponding to the thickness reduction is applied to the top edge with the same strain rate as used for polycrystalline modeling (10^{-3} s^{-1}). The right edge is free to move in the X direction. The left and bottom edges are constrained from moving in the X and Y directions, respectively. Multi-point constraints are applied to maintain the right edge straight during deformation. Aiming at an explicit understanding of the influence of the initial orientation combination on shear banding, corresponding simulations of bicrystals with various initial microstructures are performed. More specifically, simulation runs are performed for four configurations: Cu (copper orientation, $(112)[11\bar{1}]$) plus Ag $((112)[11\bar{1}])$; Cu $((112)[11\bar{1}])$ plus Ag (Goss orientation, $(011)[100]$); and Cu $((011)[100])$ plus Ag $((112)[11\bar{1}])$. In each model, the crystal is exactly oriented as an ideal component, i.e. all elements have the same initial orientation without any orientation scatter [55]. As there is an approximate assumption that plane strain conditions are valid on the bicrystals, finite element meshes with second-order isoparametric, six-noded, two-dimensional plane strain triangular elements are used. In each element the same crystallographic orientation of the crystal is assigned to its three integration points.

4.2. Orientation distribution in bicrystals

The predicted distribution of the grain rotation angle for the Cu–Ag bicrystals with various orientation combinations at ~40% thickness reduction is shown in Fig. 3a–c. The rotation angle is defined as the misorientation angle relative to the initial orientation of each crystal. It is emphasized that the principal stresses considered in the constitutive
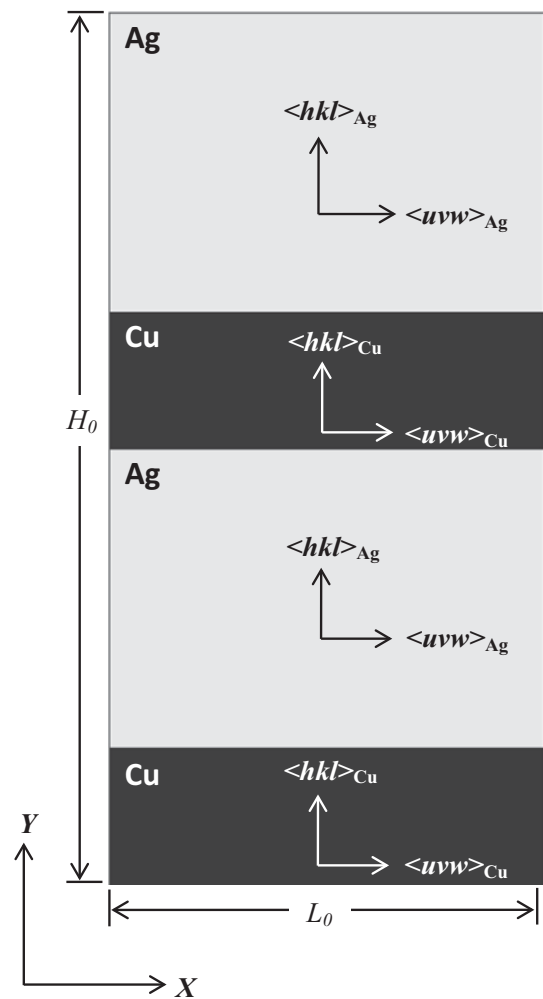

Fig. 2. Schematic of the heterophase Cu–68.3 vol.% Ag bicrystal model (Cu phase in dark gray and Ag phase in light gray). To simulate plane strain compression, a prescribed displacement corresponding to the targeted thickness reduction is applied to the top edge. The left and bottom edges are constrained from moving in the X and Y directions, respectively. The right edge is permitted to move in the X direction.

shear band model are derived by principal axis transformation from the second Piola–Kirchoff stress tensor $\mathbf{T}^e$ [16]. As the decomposition of the second Piola–Kirchoff stress is: $\mathbf{T}^e = \sum_{i=1}^{3} \sigma_i \hat{\mathbf{e}}_i \otimes \hat{\mathbf{e}}_i$ with σ_i the principal stresses and $\hat{\mathbf{e}}_i$ the orthonormal principal directions of $\mathbf{T}^e$, we order these principal stresses according to $|\sigma_1| \geqslant |\sigma_2| \geqslant |\sigma_3|$. To explore the micromechanism of lattice reorientation in the plane strain compressed samples, the simulated results in terms of the distribution of shear rate on the $(\hat{\mathbf{e}}_1 - \hat{\mathbf{e}}_3)$ shear band systems and shear stress in the plane constructed by RD and ND (σ_{13}) for each bicrystal are also presented in Fig. 3.

For the Cu (copper orientation) plus Ag (copper orientation) bicrystal (Fig. 3a), a larger lattice rotation (above 20°) is localized inside the Ag crystals as well as in that area of the Cu crystals which is connected to the abutting strain localization zone of the Ag phase. In the respective phases the material points with larger grain rotations correspond to zones with higher shear stresses. Moreover, the occurrence of localized rotation coincides with the initiation of

the shear band systems. It is found that shear bands in the upper Cu crystal are specifically triggered by stress concentrations at phase boundaries, which leads to the significant reorientation of crystalline portions within the bands. In addition, at this stage significant bending of the regions near the phase boundaries is predicted and zones of large grain rotation (~55°) penetrate through the curved heterophase boundaries. The curved phase boundaries are corresponding to the material points where shear band regions intersect the interfaces. Accordingly, the elements inside the shear bands of the Cu phase are severely narrowed, even though the Cu phase is mechanically stronger than the Ag phase. A consistent result has been observed in metallic multilayers made from dissimilar metals where shear bands running through the layers lead to necking of the respectively harder material [17,56]. The highly compacted meshes in the microstructure indicate that elements in those areas have been severely distorted.

To emphasize and visualize the microtextures in the Cu–Ag bicrystals with different microstructures more clearly, the lattice rotations along the line AB, which is parallel to the ND, are traced. As indicated in Fig. 3a–c, in each bicrystal the scanned line passes zones with large grain rotation and severe phase boundary curvature. The predicted grain rotation angle for the samples at a fixed strain is plotted as a function of the 40 evaluated points reaching from "A" to "B", as shown in Fig. 4. Equivalent true strain values are also shown in the plots against the evaluated points along each line scan. The insert in each plot is the {1 1 1} pole figure for the most heavily rotated point in the constituent phases of the deformed bicrystal. For the Cu (copper orientation) plus Ag (copper orientation) sample (Fig. 4a), the grain rotation line scan reveals large rotation spreads up to 50–55° with respect to the original orientation of each point in both phases. These rotations occur about the TD//$\langle 1 1 0 \rangle$ axis and lead to the
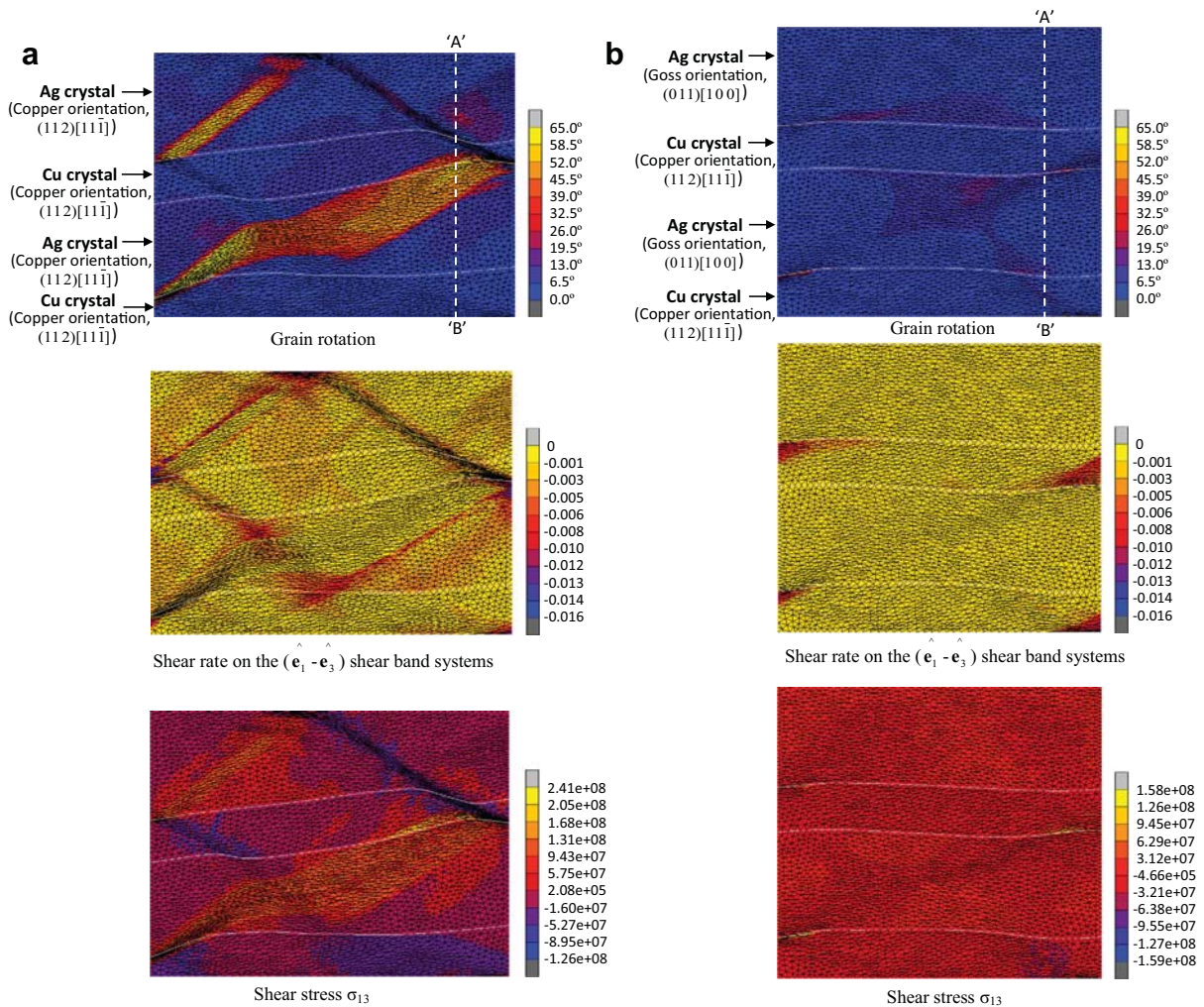

Fig. 3. Predicted distributions of grain rotation angle, shear rate on the ($\hat{e}_1 - \hat{e}_3$) shear band systems and shear stress σ_{13} for bicrystals with different initial orientations: (a) Cu (copper orientation, $(1 1 2)[1 1 \bar{1}]$) plus Ag (copper orientation, $(1 1 2)[1 1 \bar{1}]$) heterophase bicrystal at 40% thickness reduction, (b) Cu (copper orientation, $(1 1 2)[1 1 \bar{1}]$) plus Ag (Goss orientation, $(0 1 1)[1 0 0]$) heterophase bicrystal at 33% thickness reduction and (c) Cu (Goss orientation, $(0 1 1)[1 0 0]$) plus Ag (copper orientation, $(1 1 2)[1 1 \bar{1}]$) heterophase bicrystal at 40% thickness reduction. In these models, white lines indicate interfaces between abutting crystals.
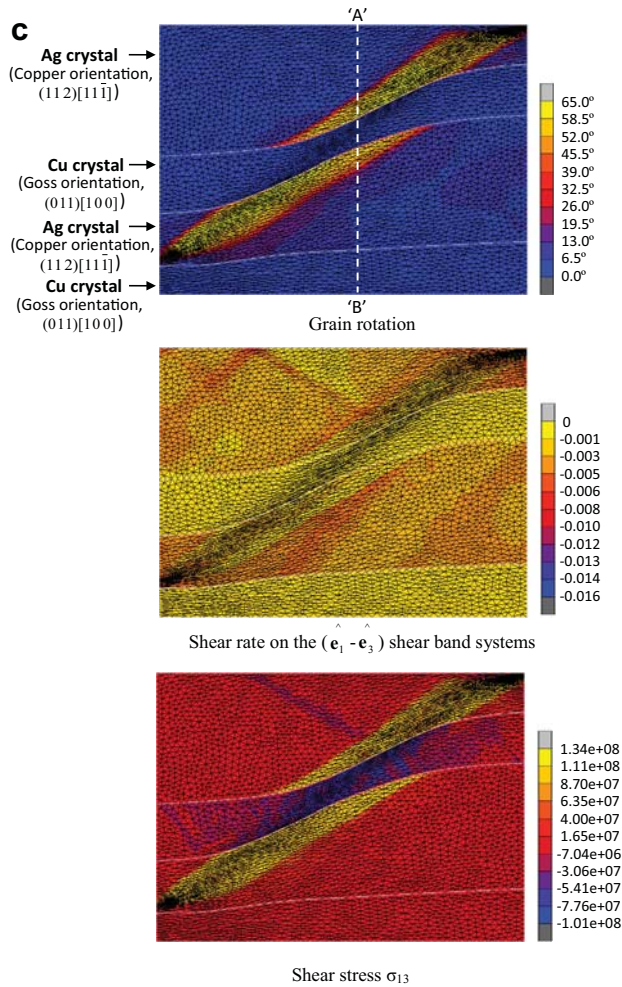
Fig 3. *(continued)*

$(4\,4\,1)[\bar{1}\,\bar{1}\,8]$ (near Goss) orientation, as shown in the corresponding pole figure. Along the line from point "A" to point "B", the change of rotation angle corresponds to the lattice rotation distribution shown in Fig. 3a. It is worth noting in that context that strain localization does not necessarily occur at the regions with large rotation angles. In the upper Cu crystal, a rotation of ~55° is identified at the phase boundary between the crystal and the lower Ag crystal. However, at the corresponding points less significant true strain (~1.5) but apparent shear banding is identified. Still in this Cu crystal, at the boundary between the crystal and the upper Ag crystal very sharp strain localization (~3.2) appears, whereas the corresponding grain rotation is below 10°. In the lower Ag crystal, the rotation angle of ~55° (corresponding to a true strain range of 0.6–1.2) occurs at the points close to the upper Cu crystal. At 20% thickness reduction we find that the shear band systems have been activated in regions of both phases where stress reaches the critical value to initiate the shear band systems. With further deformation, stress becomes homogeneously distributed throughout the bicrystal. Accordingly, decreasing shear rates of the shear band systems is predicted within the bands and activation of the shear band
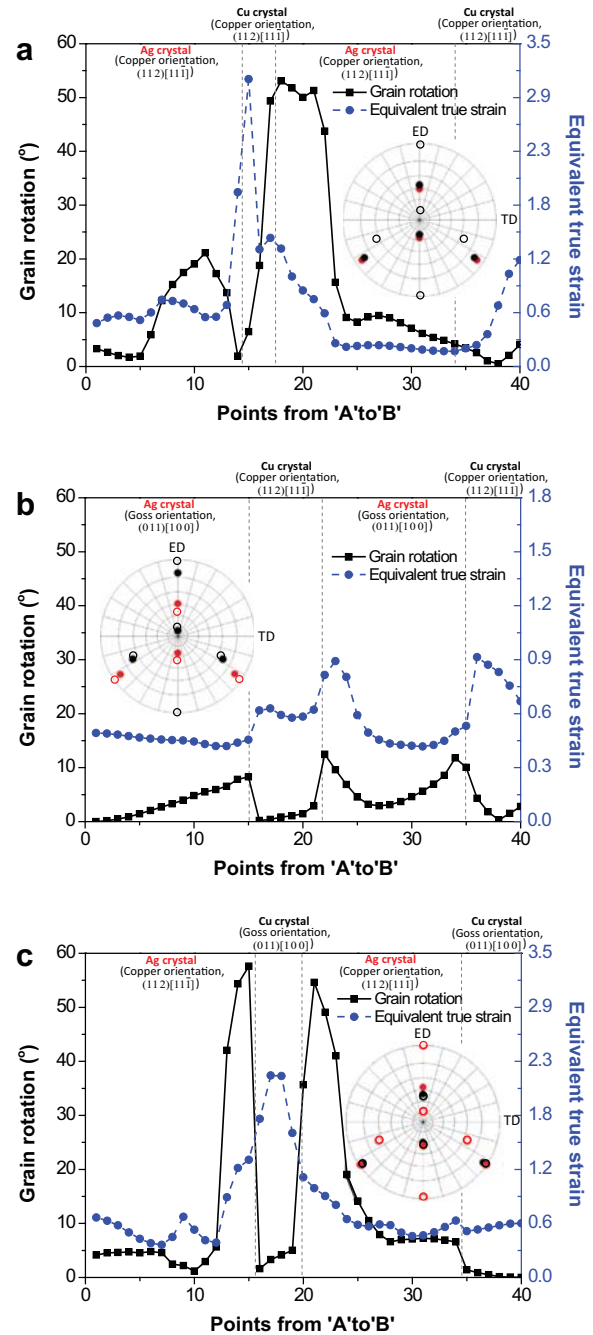

Fig. 4. Predicted evolution of grain rotation angle with respect to its original orientation and a equivalent true strain for each phase in a deformed Cu–Ag bicrystal, along the line scan from "A" to "B" (as marked in Fig. 3a–c) for the corresponding models: (a) Cu (copper orientation, $(1\,1\,2)[1\,1\,\bar{1}]$) plus Ag (copper orientation, $(1\,1\,2)[1\,1\,\bar{1}]$) heterophase bicrystal at 40% thickness reduction, (b) Cu (copper orientation, $(1\,1\,2)[1\,1\,\bar{1}]$) plus Ag (Goss orientation, $(0\,1\,1)[1\,0\,0]$) heterophase bicrystal at 33% thickness reduction and (c) Cu (Goss orientation, $(0\,1\,1)[1\,0\,0]$) plus Ag (copper orientation, $(1\,1\,2)[1\,1\,\bar{1}]$) heterophase bicrystal at 40% thickness reduction. On each line the grain rotation angle and equivalent true strain at 40 evenly distributed points are evaluated. The {1 1 1} pole figures show the initial orientation (in open circle "○") and the orientation after deformation (with the maximum rotation angle, in solid circle "●") for each phase. Orientations of the Cu and Ag phases are represented in black and red, respectively. (For interpretation of the references to color in this figure legend, the reader is referred to the web version of this article.)

systems is mainly localized at the border of the bands. Our previous simulations on Cu single crystals [57] have shown that the activation of the shear band systems enables the in-band region to be rotated around the transverse direction of the rolled sample, which then facilitates further strain accommodation by homogeneous slip along the shear plane. Consequently, the area outside the bands is gradually incorporated into the bands with deformation. This feature is extensively reported as the development of shear bands by experiments [9,14,15], and is predicted as band thickening in our simulations [57]. Therefore, at 40% thickness reduction the insignificant shear banding inside the shear banding region is attributed to the release of stress in the firstly formed shear bands. This explains the significant grain rotation but the weakly activated shear band systems inside shear bands as well as the insignificant grain rotation at the border of the continuously thickened bands with deformation. In regions far from the boundary between the upper Cu crystal and the lower Ag crystal, the rotation angle is within a range of 0–20°. This means that the Ag crystal undergoes a rotation about the $\langle 110 \rangle$ axis to reach the $(114)[\bar{2}\bar{2}1](G^T)$ orientation. In the lower Cu crystal, the rotation angle is below 10°, indicative of the stable orientation of the crystal. To this stage, a tentative conclusion is that the localized true strain does not necessarily coincide with significant lattice rotations. The deformation mechanisms (dislocation slip, twinning and shear banding) that contributes to crystallographic shear primarily determines the rotation of the crystal. Hence, to precisely capture texture evolution in a bulk material with heterophase interfaces, it is essential to understand how the strain distribution and the lattice rotations are influenced by co-deformation of the constituent phases, as will be discussed in Section 5.

For the Cu (copper orientation) plus Ag (Goss orientation) bicrystal at 33% thickness reduction, compared to the corresponding phases in the Cu (copper orientation) plus Ag (copper orientation) bicrystal, the maximum lattice rotation is lower ($\sim$25°) in both the Ag and Cu phases (Fig. 3b). Since the Cu phase has an initial orientation that promotes shear banding as shown in Refs. [16,58], the regions with larger lattice rotation in the different phases are connected with each other at those material regions of the Cu crystals where significant shear banding appears. This observation shows that the local constraints exerted from a phase with shear bands reaching a hetero-interface promote lattice rotation also in its neighbor phase. In the lower Ag crystal larger rotation is also found between the left and right edges of the crystal. However, no shear banding is activated in this phase with its initial Goss orientation. Along the line scan in this bicrystal (Fig. 4b), the distribution of true strain fluctuates although the maximum value reaches $\sim$1.0. It is generally observed that the initial textures in the respective phases rotate at higher degrees in regions with larger strain localization. In the Cu and Ag crystals, a rotation of $\sim$10° about TD//$\langle 110 \rangle$ with respect to their respective original orientations occurs

at the phase boundaries. This corresponds to the formation of the $(4411)[111\bar{1}\bar{8}](D)$ orientation in Cu and the orientation close to the $(26\,26\,5)[\bar{5}\bar{5}52](D^T)$ in Ag, respectively. In regions adjacent to the phase boundaries, the rotation angle decreases with increasing distance between the evaluated points and the boundaries. As the initial orientation of the Ag phase is not preferential for activating the shear band systems, the larger rotation ($\sim$10°) in the Ag crystals is irrelevant to shear banding. Moreover, in the Cu phase the $\sim$10° rotation does not coincide with the activation of the shear band systems either, as clearly seen at the boundary between the lower Ag and Cu crystals where no shear banding is identified (Fig. 3b). Therefore, in this sample dislocation slip is the main cause of grain rotation for both phases.

For the 40% deformed Cu (Goss orientation) plus Ag (copper orientation) sample, in the Ag phase the region with large grain rotations (above 55°) yields an angle of $\sim$37° with respect to the ED (Fig. 3c). This pattern is close to that of the copper-oriented Ag single crystal [58]. However, very minor rotation is found in the Cu phase although phase boundaries of the upper Cu crystal have been largely rotated to be approximately aligned with the rotated region in the abutting Ag crystals. This is because shear banding is only activated in the Ag phase but not in the Cu phase. In the Ag crystals shear banding is identified at the border of the zone with large rotations, suggesting that at this stage shear banding plays a major role in accommodating the imposed deformation between shear bands and regions outside the bands. The significant shear stress at the material points in the Ag crystals with large rotations indicates that the activation of the shear band systems is triggered in this phase when local stress reaches the critical value to initiate shear banding. Following the scanned line in the bicrystal (Fig. 4c), a maximum rotation about the TD up to $\sim$55° is predicted in the Ag phase. In addition, a larger true strain (above 0.6) is found at the points located within the upper Cu crystal and the points within the Ag crystals with large rotations. More specifically, 55° rotation of the Ag crystals coincides with the occurrence of shear bands and also of localized strain. In the upper Cu crystal, the rotation angle is lower than 10° although a significant local true strain of $\sim$2.2 is predicted. In this sample, the initial orientation of the Cu phase is not preferential for activating the shear band systems. Thus, the large strain in the Cu crystals is not induced by shear banding but by dislocation slip. In other regions with relatively low true strain (below 0.6) as well as insignificant shear banding, small rotations (less than 10°) are predicted in both phases.

5. Discussion

5.1. Lattice reorientation and micromechanics in heterophase MMCs

According to the bicrystal simulations, it is found that the activation of the shear band systems is related to the
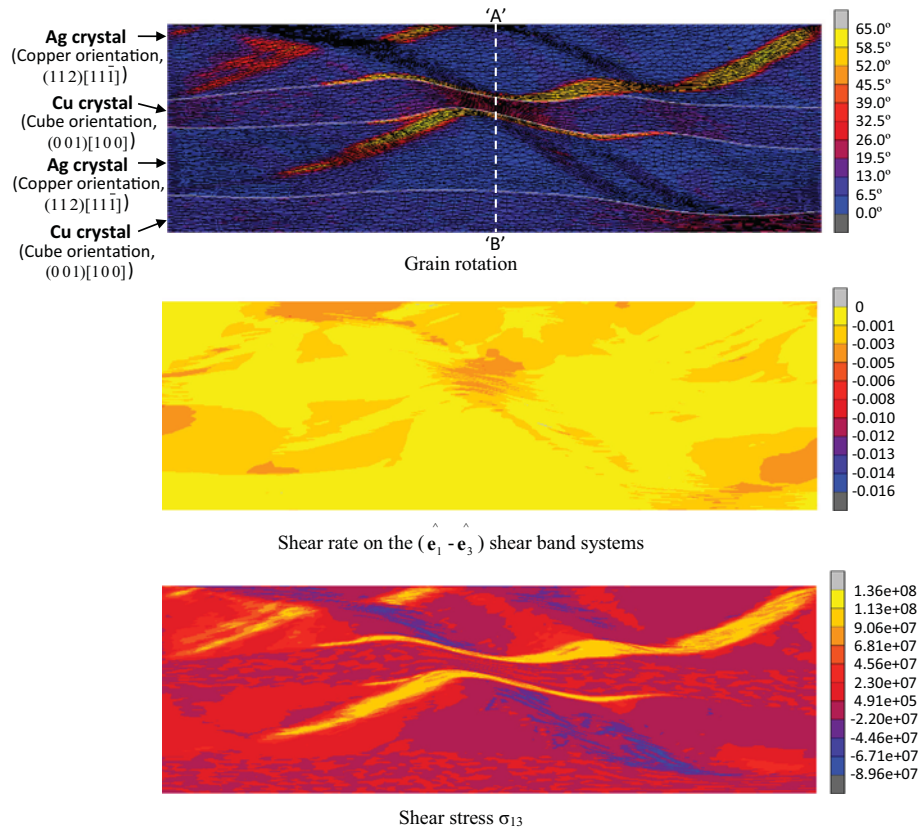
Fig. 5. Predicted distributions of grain rotation angle, shear rate on the $(\hat{e}_1 - \hat{e}_3)$ shear band systems and shear stress σ_{13} for a Cu (cube orientation, with a 10° spherical Gaussian scattering about $(0\,0\,1)[1\,0\,0]$) plus Ag (copper orientation, $(1\,1\,2)[1\,1\,\bar{1}]$) heterophase bicrystal at 60% thickness reductions. White lines indicate interfaces between the abutting crystals. Finite element mesh is only shown in the first row of results for better visibility of the distribution of shear bands.

actual topology of heterophase microstructures in addition to the crystallographic orientations of the grains involved. This is in accordance with the observation made in some single-phase metals that pre-existing anisotropic features, such as microbands or lamellar microstructures, are a necessary precursor to shear band formation [14,20]. Moreover, shear banding plays a major role in the inhomogeneous orientation distribution within the samples. To observe lattice reorientation modified by microstructures more clearly, a simulation of a Cu (cube orientation) plus Ag (copper orientation) bicrystal is performed. Under plane strain load the ideally cube-oriented fcc crystals are not susceptible to shear band formation [10,16,59]. However, if some scatter about the cube orientation is used as the initial texture of the crystals, shear banding can be triggered when a high enough stress is reached. The initial texture scatter of the Cu phase is described in the form of a spherical Gauss component [44,55,59] with a full width at half maximum of 10° about the $(0\,0\,1)[1\,1\,0]$ orientation, while the other model parameters are the same as those used for Cu–Ag samples presented above. As the shear band systems in the cube-oriented crystal are activated at a later deformation stage compared to the copper orientation, the predicted distribution of grain rotation angle, shear rate on the $(\hat{e}_1 - \hat{e}_3)$
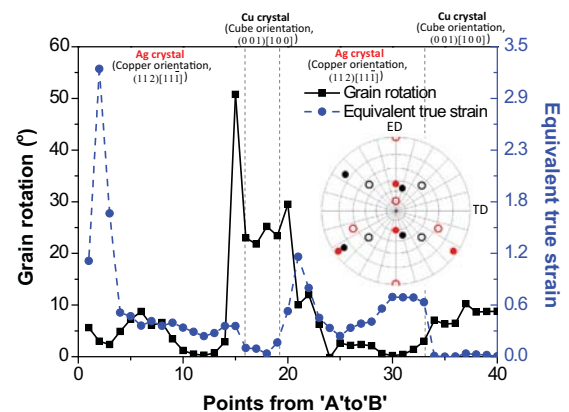

Fig. 6. Predicted evolution of grain rotation angle and equivalent true strain in a 60% deformed Cu (cube orientation, with a 10° spherical Gaussian scattering about $(0\,0\,1)[1\,0\,0]$) plus Ag (copper orientation, $(1\,1\,2)[1\,1\,\bar{1}]$) bicrystal, along the line scan from "A" to "B" (as marked in Fig. 5). On the line the grain rotation angle and equivalent true strain at 40 evenly distributed points are evaluated. The {1 1 1} pole figures show the initial orientation (in open circle "○") and the orientation after deformation (with the maximum rotation angle, in solid circle "●") for each phase. Orientations of the Cu and Ag phases are represented in black and red, respectively. (For interpretation of the references to color in this figure legend, the reader is referred to the web version of this article.)

shear band systems and shear stress σ_{13} for the Cu (cube orientation, with a 10° scatter) plus Ag (copper orientation, $(1\,1\,2)[1\,1\,\bar{1}]$)) bicrystal at 60% deformation is presented (Fig. 5). In the Ag crystals large rotations (above 50°) are observed, while in the Cu crystals the area connected to the localization of the Ag phase shows a lattice rotation above 20°. Shear banding is clearly identified at the region with larger rotations in the respective phases. These shear bands induce severe curvature of the phase boundaries. Moreover, in both phases the area with larger stress coincides with the material points where shear banding initiates. This again causes shear bands in the upper Cu crystal to be triggered by such stress concentration near phase boundaries. To this stage, a curved lamellar structure is predicted as a result of local plastic instability in the shear banding region. This phenomenon agrees very well with experimental observations reported on cold rolled Cu–Ag [11,48] and Cu–Nb [20,49] composites with layered structures.

The lattice rotation as well as the equivalent true strain in the bicrystal along the line AB which is parallel to the ND (Fig. 5) is traced, as shown in Fig. 6. In the Ag phase, larger rotations (above 10°) are seen in the region close to the phase boundaries. At the bottom of the upper Ag crystal, the TD rotation reaches ~55°, while at the top of the lower Ag crystal, the rotation about the TD is ~30°. These rotations lead to the formation of the $(1\,1\,0)[0\,0\,1]$ and $(3\,3\,2)[1\,1\,\bar{3}]$ orientations, respectively. By examining the distribution of shear rate of the shear band systems, it is obvious that at this deformation stage the initial copper texture in the Ag phase rotates about the TD towards the Goss component with significant shear induced by shear banding. In regions with weak shear banding, the maximum rotation in the Ag crystals is ~10°, although a strong true strain localization of ~3.0 is identified at those points, e.g. the second top point in the upper Ag crystal. For the Cu phase, in the upper crystal showing the activation of shear banding, a larger rotation value is observed. The associated rotations towards Goss occur as shown in the pole figure, i.e. the initial $(0\,0\,1)[1\,1\,0]$ orientation undergoes a ~33° rotation about the ED//$\langle 1\,0\,0 \rangle$ axis to reach the $(0\,2\,3)[1\,0\,0]$ orientation. In the lower Cu crystal where very weak shear banding is activated, the resultant orientation corresponds to a rotation of ~10° to $(0\,1\,4)[1\,0\,0]$. Therefore, in the Cu crystals the large rotations observed about the ED are associated with the occurrence of shear bands. This interpretation is also confirmed by microtexture measurements on a channel-die compressed Cu cube crystal showing well-developed shear bands [60]. Hence, the behavior of the cube oriented Cu crystal can be described in the following way. When the thickness reduction is low (below 60%), shear banding is only activated in the Ag phase and no shear banding occurs in the Cu phase. The activation of the shear band systems in the Ag phase enables the lattice to be rotated about the TD anti-clockwise, which also imposes a TD rotation on the upper Cu crystal embedded between the Ag crystals. That is to say,

the TD rotation in the Cu phase originates from a rigid-body rotation induced by the abutting Ag crystals; therefore, its value would also be small (below 10°). With increasing deformation, shear banding is triggered in the Cu phase at the material points adjacent to the already-activated bands in the Ag phase. More specifically, shear bands "seem" to run across the phase boundaries and extend into the Cu crystals. This leads to the reorientation of the shear banding region in the Cu phase. At the same time, the second shear band that is roughly symmetric to the firstly formed band rotated about the ND appears in the Ag phase, causing the strain localized region in both phases to rotate clockwise about TD. These rotations, together with the rotation occurring at small strains, contribute to the significant rotation angle of the upper Cu crystal (above 20°) and the inclined grain boundaries, as shown in Fig. 5.

It is well known that cube-oriented crystals in fcc metals are metastable during near-plane strain deformation, depending on the exact boundary conditions imposed during loading [10,16,57,61]. There are four slip system with maximum orientation factor for the cube orientation, i.e. $(1\,1\,1)[1\,0\,\bar{1}]$, $(\bar{1}\,\bar{1}\,1)[\bar{1}\,0\,\bar{1}]$, $(\bar{1}\,1\,1)[\bar{1}\,0\,\bar{1}]$ and $(1\,\bar{1}\,1)[1\,0\,\bar{1}]$. According to the current simulation, when the thickness reduction is below ~40% (0.51 true strain), in the Cu phase only dislocation slip occurs. At higher deformations, our prediction clearly demonstrates the formation of shear banding in the Cu phase, while the above-mentioned slip systems become less active in the shear bands. Due to an increase of the Schmid factor on the reoriented {111} plane, two new slip systems $((\bar{1}\,\bar{1}\,1)[1\,1\,0]$ and $(\bar{1}\,1\,1)[1\,1\,0])$ are activated in the shear banding region. These newly activated slip systems lead to the predominant rotation about the ED and accordingly the cube texture is rotated towards the Goss position. This case has been experimentally verified by an investigation on the evolution of rolling textures in fcc metals with initial cube texture [62], and explicitly stated as a correlation to the formation of microshear bands [60]. Finally, note that in this simulation, the hetero-phase boundaries experience severe curvature and the lattice rotation is strongly affected by the shear banding behavior of the constitutive phases, as also predicted for other bicrystals (Fig. 3), indicating the ubiquitous nature of the phenomenon.

5.2. Texture evolution with shear banding

As revealed by experiments for the same type of Cu–Ag composite as studied in this work, after rolling to various thickness reductions the Cu and Ag phases develop similar textures, i.e. less copper-type and instead more brass-type components [26]. Moreover, a similar texture evolution showing a low volume fraction of the copper and S components is also observed in the Cu phase of the Cu–Nb composite [20]. These results are not a priori expected because in single-phase Cu under the same rolling conditions, the copper-type rather than the brass-type textures have been
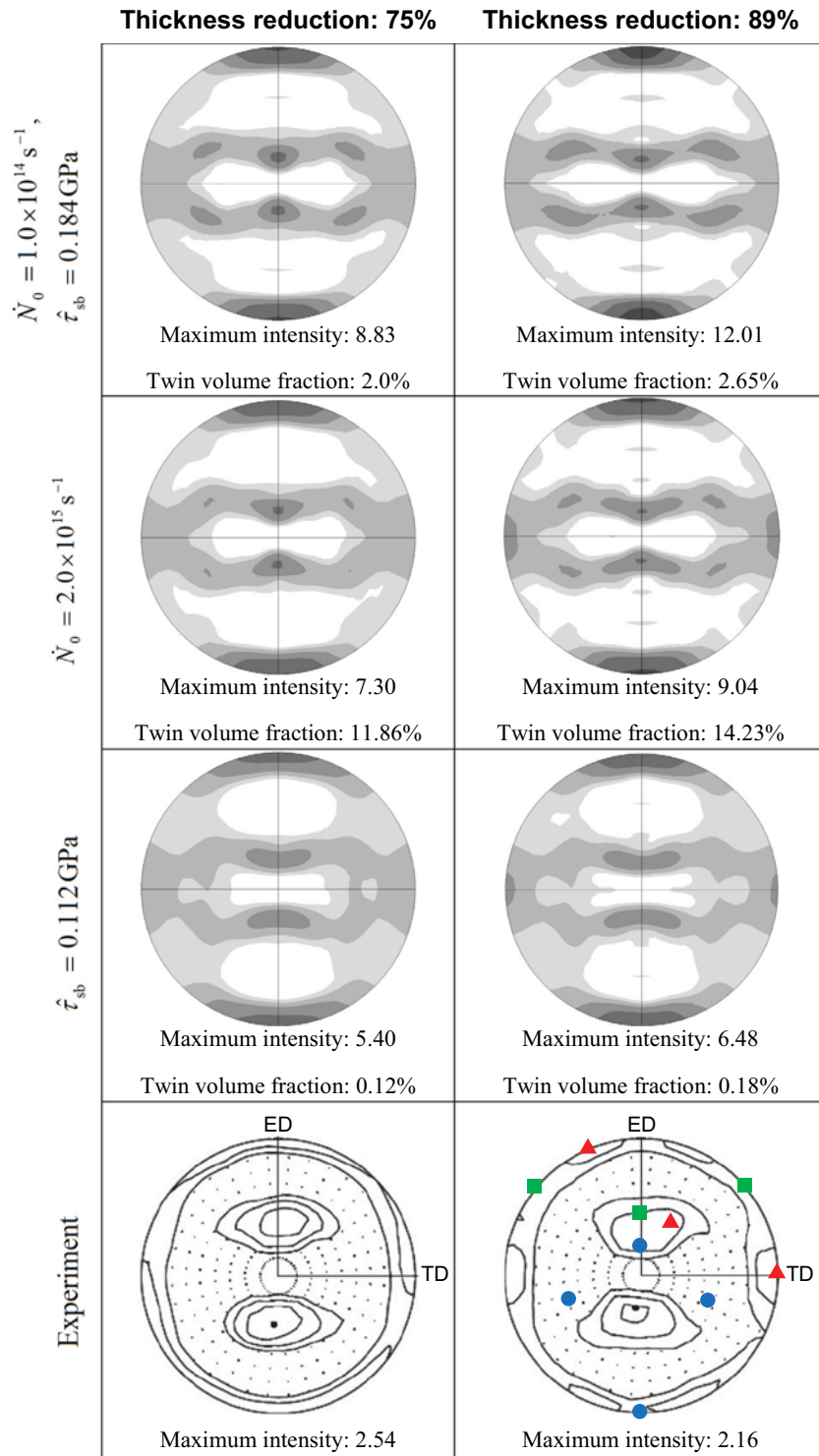
Thickness reduction: 75%   **Thickness reduction: 89%**

Fig. 7. Polycrystal model predicted and experimental {111} pole figures of the Cu phase in Cu–68.3 vol.% Ag composite at different thickness reductions. The experimental data is obtained from Ref. [26]. (●) Copper orientation ({112}⟨111⟩), (■) Goss orientation ({011}⟨100⟩), (▲) brass orientation ({011}⟨211⟩).

reported to be typically developed [2,4,54]. Thus, the experimental measurements conducted on composites indicate that the existence of the abutting phase or the interface between phases plays an important role in the texture

development of the Cu phase within composite materials. However, this feature is not captured by the polycrystalline model presented above. Considering the characteristic texture evolution in the Cu–Ag composite as obtained by
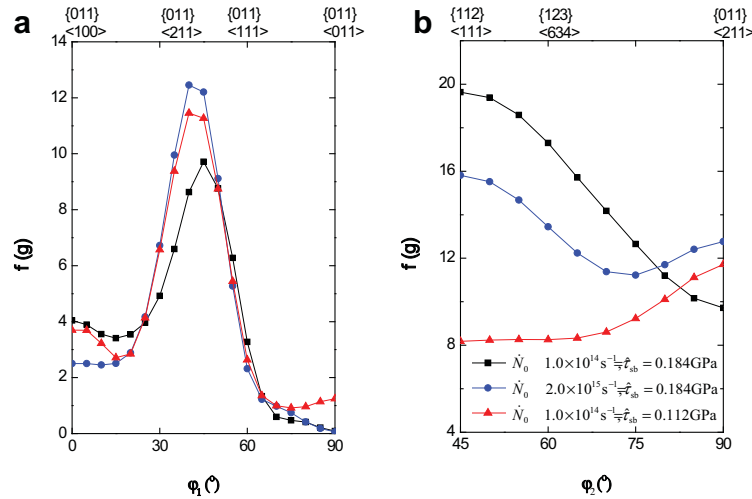
Fig. 8. Polycrystal model predicted texture evolution of the Cu phase in Cu–68.3 vol.% Ag composite at 89% thickness reduction in (a) α and (b) β fiber representation.

experiments, two main analyses apply: (1) the Cu phase deforms via similar relative contributions of dislocation slip and twinning as the Ag phase. In the Cu phase twinning would also contribute to the formation of brass-type textures. However, some prior studies place this idea in question, because in either cold rolled Cu–Ag or Cu–Nb composites with a starting layer thickness in the submicron regime [26,63] mechanical twinning is not identified as an important deformation mechanism in the Cu phase, at least not at modest strains such as imposed here. (2) For fcc materials, at large deformations non-crystallographic deformation in the form of shear banding can be initiated by a mechanical instability that contains band-like dislocation cells in high-SFE metals [18,64] or twin-matrix lamellae in low-SFE metals [1,2,8,9]. In both cases, shear banding leads to a weaker copper-type but stronger brass-type texture. This would mean that in the Cu phase of the studied Cu–Ag composite more shear banding may be activated compared to pure Cu. On the other hand, a more detailed analysis of the orientation distributions in a variety of bicrystal samples reveals that lattice rotation in the Cu phase is significantly influenced by the interface between the abutting phases. To accommodate deformation between hetero-phases, pronounced shear bands are triggered by stress concentration at the interfaces, i.e. phase boundaries. This leads to highly localized strains and lattice reorientations within the bands. According to the bicrystal simulations, in the Cu–Ag samples the ~55° rotation of the copper-oriented Cu crystal coincides with the activation of the shear band systems and leads to a texture component close to the Goss orientation. Concerning the set-up of the polycrystal and the bicrystal models, in both cases only one single phase and one orientation are assigned to the respective integration points. Therefore, the different micromechanisms as revealed by the different texture evolutions between the different modeling methods

occur primarily because in the former case the phases are randomly arranged within the polycrystal, whereas in the latter case they are mutually stacked to model the lamellar structure typically found in real Cu–Ag composites [48,49]. Moreover, using the Taylor assumption the polycrystalline simulations do not exactly mimic the strong boundary constrains of individual crystals as that imposed by the bicrystal model. These dissimilarities lead to the minor shear banding activity triggered from the presence of heterophase interfaces when implementing polycrystalline modeling.

To demonstrate the shear banding effect on texture development in the Cu phase of the Cu–Ag composite, we reduce the activation stress for shear banding ($\hat{\tau}_{sb}$) of Cu from 0.184 GPa down to 0.112 GPa in the polycrystal simulation. Fig. 7 shows {1 1 1} pole figures of the Cu phase at 75% and 89% rolling reductions predicted by the different simulations. For comparison, the modeling using an increased initial nucleation rate for twinning ($\dot{N}_0$) [16] as well as the experimental results [26] are also presented. At corresponding deformation stages the predicted twin volume fractions in the Cu phase are given. Comparing the simulations with different threshold stress for shear banding, it is seen that at 75% deformation an easier activation of the shear band systems ($\hat{\tau}_{sb} = 0.112$ GPa) leads to a suppression of the development of the copper component, and with increasing deformation this suppression becomes more pronounced. In addition, stronger brass-type textures are predicted when using a 0.112 GPa activation stress, as seen from the α and β fibers at 89% deformation in Fig. 8. When an initial twin nucleation rate of 2.0×10^{15} s^{-1} is used, the simulation predicts the suppression of the texture evolution towards the copper component and a strengthening of the brass-type texture. This means that the textures are influenced by an increase of the twin volume fraction to an extent of ~11%. However, compared to the simulation

using 0.112 GPa activation stress for shear banding the model with higher twin nucleation rate ($\dot{N}_0 = 2.0 \times 10^{15}$ s^{-1}) shows a weaker suppression of the copper component, although in the former case only very weak deformation twinning occurs. Therefore, the prediction incorporating more non-crystallographic shear contributions reproduces experimental textures of the composite better.

In fact, the texture development in plane strain deformed lamellar composites is a clear example of the effect of the co-deformation mechanisms on texture evolution in heterophase microstructures. In this work, lattice rotations in a Cu–Ag composite are studied by performing a series of simulations for bicrystal configurations with specific/ideal crystallographic orientation combinations. Simulations of the texture evolution in polycrystalline composites without considering the initial heterophase microstructures are also presented for comparison. Although gross simplifications in terms of capturing initial microstructures (crystal morphology and crystal orientation) and setting boundary conditions have been made in the current bicrystal simulations, the localized stress and strain distributions as well as the co-deformation mechanisms within heterophase microstructures have been revealed. One of the important findings is that for each individual crystal, the actual presence of abutting crystals of another phase influences its shear banding behavior and thus leads to the texture transition of the crystal affected from the copper-type to the brass-type. For accurately predicting textures of bulk composite materials under loading, the accurate initial microstructures should be incorporated in the models. Besides, an in-depth investigation that includes deformation mechanisms occurring within realistic microstructure topologies is required. For instance, for modeling nanoscale multilayer composites in which heterophase interfaces confine slip to crystallographic planes closely aligned with the interface planes, the numerical model should also account for the effects of confined layer slip and dislocation transmission across interfaces [12,64–66] on the texture evolution. Experimental investigations and simulations at the atomic scale [67–69] are essential for elucidating the structures of heterophase interfaces and the localized stress and strain fields when under load, thus guiding and informing the development of an advanced mesoscopic model for predicting textures and more complex microstructures. However, these are beyond the scope of the current paper.

6. Conclusions

We have presented crystal plasticity finite element simulations of the texture evolution in plane strain compressed Cu–Ag polycrystalline MMC. Comparisons of the simulated and experimental textures were conducted and quantitatively evaluated. Simulations based on bicrystal models considering characteristic initial heterophase microstructures of the composite were performed in order to reveal lattice rotations, shear banding behavior and the underlying micromechanics. The main results are as follows:

- Using the polycrystal model, the Goss, brass, copper and S texture components are predicted in both phases of the composite at 50% thickness reduction. With further deformation, the copper and S components significantly increase in the Cu phase and the resultant textures are of the copper-type. This result deviates from experimental measurements that reveal brass-type textures in the composite at 75% and higher deformations. In the Ag phase, significant development of the brass and Goss components is predicted, which matches experimental measurements.

- The bicrystal simulations reveal that significant non-crystallographic shear banding occurs in the fcc crystals, depending on the specific initial orientations. In the Cu–Ag composite, for crystals initially oriented with copper of either phase, the ~55° rotation about the $\langle 110 \rangle$ axis coincides with the activation of shear banding and the resultant texture is close to the Goss component. On the other hand, less rotation (below 10°) occurs when the plane strain deformation is mainly assisted by dislocation slip and twinning.

- The bicrystal simulations reproduce the experimentally observed trends of texture evolution in the respective phases of the Cu–Ag composite. This indicates that the localized stress and strain fields as well as the co-deformation mechanisms within the actual heterophase microstructures are well captured by the bicrystal modeling. To accommodate deformation between adjacent phases in the bicrystal samples, pronounced shear bands are triggered by stress concentration at phase boundaries. These bands penetrate through the phase boundaries with deformation, leading to the highly localized strain and promoting lattice reorientations in the neighbor phase. The initial orientation of each individual crystal and mechanical properties of the abutting crystals are the most important factors in affecting shear band development and the associated texture evolution.

- We thus conclude that the main deformation mechanism in heterophase MMCs is different from that in single-phase metals. Also the texture evolution in composite materials is strongly influenced by the local constraints exerted from the immediate presence of hetero-interfaces and the abutting phases. By incorporating more non-crystallographic shear contributions in an individual phase of the composite, polycrystalline simulations capture the experimental textures. This suggests that for modeling deformation textures in heterophase microstructures, the localized stress and strain fields that exhibit a strong influence on the shear banding behavior have to be precisely predicted.

References

[1] Duggan BJ, Hatherly M, Hutchinson WB, Wakefield PT. Metal Sci 1978;12:343.
[2] Hirsch J, Lücke K. Acta Metall 1988;36:2863.
[3] Ushioda K, Hutchinson WB. ISIJ Int 1989;29:862.
[4] Donadille C, Valle R, Dervin P, Penelle R. Acta Metall 1989;37:1547.
[5] Wagner P, Engler O, Lücke K. Textures Microstruct 1991;14:927.
[6] Tvergaard V, Needleman A. Proc R Soc London A 1993;443:547.
[7] Paul H, Driver JH, Maurice C, Jasieński Z. Mater Sci Eng A 2003;359:178.
[8] Paul H, Morawiec A, Bouzy E, Fundenberger JJ, Pia A. Metall Mater Trans A 2004;35:3775.
[9] Paul H, Driver J, Maurice C, Piatkowski A. Acta Mater 2007;55:575.
[10] Kuroda M, Tvergaard V. Int J Plast 2007;23:244.
[11] Davy CA, Han K, Kalu PN, Bole ST. IEEE Trans Appl Supercond 2008;18:560.
[12] Li YP, Tan J, Zhang GP. Scr Mater 2008;59:1226.
[13] Xiao GH, Tao NR, Lu K. Scr Mater 2008;59:975.
[14] Paul H, Morawiec A, Driver JH, Bouzy E. Int J Plast 2009;25:1588.
[15] Hong CS, Tao NR, Huang X, Lu K. Acta Mater 2010;58:3103.
[16] Jia N, Roters F, Eisenlohr P, Kords C, Raabe D. Acta Mater 2012;60:1099.
[17] Govindaraj NV, Frydendahl JG, Holmedal B. Mater Des 2013;52:905.
[18] Duckham A, Knutsen RD, Engler O. Acta Mater 2001;49:2739.
[19] Nguyen-Minh T, Sidor JJ, Petrov RH, Kestens LAI. Scr Mater 2012;67:935.
[20] Raabe D, Ball J, Gottstein G. Scr Metall Mater 1992;27:211.
[21] Bolmaro RE, Browning RV, Guerra FM, Rollett AD. Mater Sci Eng A 1994;175:113.
[22] Mecking H, Seeger J, Hartig C, Frommeyer G. Mater Sci Forum 1994;157–162:813.
[23] Akdut N, Foct J. Scr Metall Mater 1995;32:103.
[24] Anderson PM, Bingert JF, Misra A, Hirth JP. Acta Mater 2003;51:6059.
[25] Belyakov A, Kimura Y, Tsuzaki K. Acta Mater 2006;54:2521–32.
[26] Beyerlein IJ, Mara NA, Bhattacharyya D, Alexander DJ, Necker CT. Int J Plast 2011;27:121.
[27] Carpenter JS, Vogel SC, LeDonne JE, Hammon DL, Beyerlein IJ, Mara NA. Acta Mater 2012;60:1576.
[28] Lee SB, LeDonne JE, Lim SCV, Beyerlein IJ, Rollett AD. Acta Mater 2012;60:1747.
[29] Kalidindi SR, Bronkhorst CA, Anand L. J Mech Phys Solids 1992;40:537.
[30] Bronkhorst CA, Kalidindi SR, Anand L. Philos Trans R Soc London A 1992;341:443.
[31] Beaudoin AJ, Dawson PR, Mathur KK, Kocks UF, Korzekwa DA. Comput Methods Appl Mech Eng 1994;117:49.
[32] Becker R, Panchanadeeswaran S. Acta Metall Mater 1995;43:2701.
[33] Clausen B, Lorentzen T, Leffers T. Acta Mater 1998;46:3087.
[34] Dawson PR, Marin EB. Adv Appl Mech 1998;34:77.
[35] Kalidindi SR. J Mech Phys Solids 1998;46:267.
[36] Staroselsky A, Anand L. J Mech Phys Solids 1998;46:671.
[37] Myagchilov S, Dawson PR. Modell Simul Mater Sci Eng 1999;7:975.
[38] Kalidindi SR. J Int Plast 2001;17:837.
[39] Raabe D, Mattissen D. Acta Mater 1998;46:5973.
[40] Mattissen D, Raabe D, Heringhaus F. Acta Mater 1999;47:1627.
[41] Raabe D, Miyake K, Takahara H. Mater Sci Eng A 2000;291:186.
[42] Jia N, Lin Peng R, Wang YD, Johansson S, Liaw PK. Acta Mater 2008;56:782.
[43] Hartig C, Mecking H. Comput Mater Sci 2005;32:370.
[44] Roters F, Eisenlohr P, Hantcherli L, Tjahjanto DD, Bieler TR, Raabe D. Acta Mater 2010;58:1152.
[45] Anand L, Su C. J Mech Phys Solids 2005;53:1362.
[46] Wang YM, Chen MW, Zhou FH, Ma E. Nature 2002;419:912.
[47] Kuhlmann-Wilsdorf D, Wilsdorf H. Acta Metall 1953;1:394.
[48] Ohsaki S, Kato S, Tsuji N, Ohkubo T, Hono K. Acta Mater 2007;55:2885.
[49] Raabe D, Heringhaus F, Hangen U, Gottstein G. Z Metallkd 1995;86:405.
[50] Wagner P, Engler O, Lücke K. Acta Metall Mater 1995;43:3799.
[51] Raabe D. Acta Metall Mater 1995;43:1023.
[52] Raabe D. Acta Mater 1997;45:1137.
[53] Dillamore IL, Roberts WT. Acta Metall 1964;12:281.
[54] Kocks UF, Tomé CN, Wenk HR. Texture and Anisotropy. Cambridge: Cambridge University Press; 1998.
[55] Raabe D, Roters F. Int J Plast 2004;20:339.
[56] Hebert RJ, Perepezko JH. Scr Mater 2004;50:807.
[57] Jia N, Eisenlohr P, Roters F, Raabe D, Zhao X. Acta Mater 2012;60:3415.
[58] Jia N, Roters F, Eisenlohr P, Raabe D, Zhao X. Acta Mater 2013;61:4591.
[59] Raabe D, Zhao Z, Roters F. Scr Mater 2004;50:1085.
[60] Basson F, Driver JH. Acta Mater 2000;48:2101.
[61] Hölscher M, Raabe D, Lücke K. Acta Metall 1994;42:879.
[62] Mao W. Chin J Met Sci Technol 1990;6:325.
[63] Misra A, Hirth JP, Hoagland RG, Embury JD, Kung H. Acta Mater 2004;52:2387.
[64] Quadir MZ, Ferry M, Al-Buhamad O, Munroe PR. Acta Mater 2009;57:29.
[65] Misra A, Hirth JP, Hoagland. Acta Mater 2005;53:4817.
[66] Li YP, Zhang GP. Acta Mater 2010;58:3877.
[67] Han WZ, Carpenter JS, Wang J, Beyerlein IJ, Mara NA. Appl Phys Lett 2012;100:011911.
[68] Wang J, Misra A, Hoagland RG, Hirth JP. Acta Mater 2012;60:1503.
[69] Yan JW, Zhu XF, Yang B, Zhang GP. Phys Rev Lett 2013;110:155502.